HIERARCHICAL COIVD FEATURE EXTRACTION AND CLASSIFICATION USING OPTIMISED JCS

[1]B. Venkateswramma,[2]D. Surendra,[3]P Jyothi Prakash ReddY,[4]Gongati Suma

[1,2,3]Assistant Professor, Department of ECE, Gouthami Institute Of Technology & Management For Women, Proddatur, Ysr Kadapa, A.P

[4]Student, Department of ECE, Gouthami Institute Of Technology & Management For Women, Proddatur, Ysr Kadapa, A.P

ABSTRACT:

The novel corona virus disease 2019 (COVID-19) has been a severe health issue affecting the respiratory system and spreads very fast from one human to other overall countries. For controlling such disease, limited diagnostics techniques are utilized to identify COVID-19 patients, which are not effective. To hinder the terrific infection of COVID-19, medical radiology imaging is employed as a complementary tool for the RT-PCR test. The above complex circumstances need to detect suspected COVID-19 patients based on routine techniques like chest CT Scans or CT scan analysis immediately through computerized diagnosis systems such as mass detection, segmentation, and classification. JCS system consists of an explainable classification branch to identify the COVID-19 opacifications and a segmentation branch to discover the opacification areas. The classifier is trained on many images with low-cost patient-level annotations and some images with pixel-level annotations for better activation mapping. And the segmentation branch is trained with accurately annotated CT images, performing fine-grained lesion segmentation. By integrating the two models, our JCS system provides informative diagnosis results for COVID-19. The image of the chests is used for mass detection using the deep learning YOLO technique. Here, it identifies the corona virus-affected chest regions from the normal tissue.

Keywords: diagnostics, COVID-19, pixel-level annotations, YOLO, Middle East Respiratory Syndrome.

I.INTRODUCTION:

In December 2019, a novel corona virus, named SARS-CoV-2, emerged in Wuhan, China, which caused the COVID-19 disease when infecting humans. COVID-19 is a serious illness that can lead to the death of the infected host [1]. The threat posed by COVID-19 led the World Health Organization (WHO) to declare the COVID-19 pandemic by March 2020 [2]. Corona viruses are a group of highly diverse, enveloped, positive-sense, single-stranded RNA,viruses and are widely spread in birds and mammals. Sometimes these viruses infect humans, causing mild to moderate respiratory diseases [3]. Before SARS-CoV-2, two corona viruses were known to cause severe human disease: SARS-CoV, which causes Severe Acute Respiratory Syndrome (SARS); and MERS-CoV, which causes Middle East Respiratory Syndrome (MERS) [4, 5]. However, in contrast to SARS and MERS, the symptom onset for COVID-19 is significantly larger, or it may appear in a mild form, allowing infection spread by asymptomatic patients, which in turn has led to the current pandemic [6]. Although the WHO has emphasized the need for massive testing and contact tracing to better tackle the pandemic, not all countries have the required laboratory infrastructure and reagents to effectively address this task. Additionally, getting results from some of these tests may take a couple of days, leading to non-confirmed COVID-19 patients with mild or no symptoms to further spread the disease while waiting for the test results. With the rise of deep learning techniques, medical imagery has increasingly claimed attention for the computed assisted analysis of pulmonary conditions. Automated analysis of Computed Tomography (CT) scans, has enabled the identification of malignant nodules [7]. Radio graphic analysis, in turn, has also obtained fair results in the detection of tuberculosis signs [8], as well as other multiple cardio-thoracic abnormalities [9, 10].

II.LITERATURE SURVEY:
COVID-19 has to be detected properly without any negligence else can lead to a severe impact on the country's economy and country's citizen health [5]. The person who is suspicious of COVID-19 is suggested to undergo a chest CT Scan. Analysis of CT Scans by humans can lead to various human errors, which can lead to a huge impact on patients and society. So, a computer-aided system can help the doctors for proper analysis of chests of the COVID-19 affected human. Throughout underdeveloped and developing nations, where the number of patients is high and medical care cannot be adequately delivered, these programs may be a tremendous benefit [6, 7]. The authors have worked on CT Scan imaging techniques for the detection of bone fractures. They have applied edge detection and segmentation techniques to ease the process of the diagnosis system. These methods will reduce the processing time and other physical evaluation procedures [8]. So, while working with CT Scan images, we need to consider the noises which have to be reduced. The random noises occurring during the process of image acquisition degrades the image quality leading to an incorrect diagnosis. Researchers

suggest the application of the temporal recursive filter. Also, they propose an improved self-adaptive filter. This was a combination of FPGA with image processing techniques [9]. The authors have recommended region localization which offers a close level of precision. Few other image preprocessing techniques are adaptive histogram-based equalization, adaptive contrast enhancement, and histogram equalization. There is the presence of multiple noises during capturing the images because of device mobility and motion artefact [10]. But in CT Scan images mostly Gaussian, salt and pepper noises are present. To reduce the noise, a digital median filtering technique is used as per the researches. Chest CT Scans aid in the diagnosis of pneumonia. Researchers seek the help of CNN in classifying normal and abnormal CT Scans [11]. The feature extracted from the chest CT Scan improves the functionality of the classifier. This method is useful where a large dataset is received. In another similar work, deep learning techniques are applied for the analysis of chest CT Scans. Pulmonary infections are easily identified using these radiography images. This is extended in the detection of corona virus disease [12].

III.EXISTING TECHNIQUE:

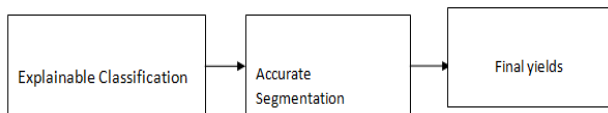### JOINT CLASSIFICATION AND SEGMENTATION:

Fig 1: Block diagram of existing technique

JCS system consists of an explainable classification branch to identify the COVID-19 opacifications and a segmentation branch to discover the opacification areas. The classifier is trained on many images with low-cost patient-level annotations and some images with pixel-level annotations for better activation mapping. And the segmentation branch is trained with accurately annotated CT images, performing fine-grained lesion segmentation. By integrating the two models, our JCS system provides informative diagnosis results for COVID-19.

EXPLAINABLE CLASSIFICATION Owing to the strong representation ability of CNNs, the COVID-19 infections can be predicted through only patient-level supervised training. To this end, we build a classification branch that consists of the proposed classification model to endow our JCS diagnosis system with the capability of discriminating the COVID-19 patients. 1) Diagnosing COVID-19 via Classification: Predicting whether the suspected patient is COVID-19 positive or not is a binary classification task based on his/her CT scan images. Since designing the novel classification model is not our focus, we build our classifier based on the Res2Net network [40]. As a powerful network, Res2Net has a stronger multi-scale representation ability than ResNet [40]. The last layer is modified as a fully-connected layer with two channels to output the probability of COVID-19 infection or not. If the probability of the infected channel is larger than that of the uninfected one, the patient is diagnosed as COVID-19 positive, or vice versa. For each patient, the CT images are sent to the classification model one by one. If the number of infected CT images is above a threshold, the patient is diagnosed as COVID-19 positive

PIXEL-LEVEL SUPERVISION FOR ACTIVATION MAPPING:

Traditional classification models only utilize image labels for training. The activation mapping of them may be inaccurate as these models automatically learn the differences of images of different classes. In our proposed dataset, there are thousands of images with pixel-level annotations for the specific opacification areas, and they can be the direct supervision of the activation mapping. Motivated by the above observations and the work of [65], during the training network, we apply a segmentation loss Lseg for the activation mapping of the COVID-19 class channel:

$$L_{seg} = \frac{1}{HW}\|AM_{p,c}^{norm} - S\|_2,$$

where AMnorm p,c is the activation mapping of the COVID-19 class channel normalized to (0, 1), S is the binary ground truth pixel-level annotation map, 2 denotes the 2 norms. Lseg will not be computed if images have no ground truth pixel-level annotations. After applying the segmentation loss Lseg, Fig. 9 shows that the activation mapping significantly improves in locating opacifications.

PROPOSED METHOD:

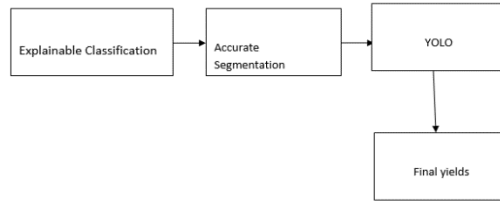**JOINT CLASSIFICATION AND SEGMENTATION WITH YOLO:**

Fig 2: Block diagram of proposed technique

The image of the chests is used for mass detection using the deep learning YOLO technique. Here, it identifies the corona virus-affected chest regions from the normal tissue.

EXPLANATION BY ACTIVATION MAPPING: As the diagnosis process of CNN classification is in a black box, we employ the activation mapping [20] to increase the explainable transparency of our COVID-19 diagnosis system on its predictions. The last convolutional layer of the classification network is followed by a global average pooling (GAP) layer and a fully-connected layer. Through the GAP layer, our classification model down-samples the feature size from (H, W) to (1, 1), and thus lost the spatial representation ability. Through activation mapping [20], our system finds the response region of the prediction result. The hypothesis is that the gradient of regions in features before the GAP layer is consistent with the prediction evidence. The feature map before the GAP layer contains both high-level semantic and location information. Each channel corresponds to the activation of different semantic cues. The activation mapping is obtained through the gradients of the predicted probability of the feature map. Specifically, given the prediction of COVID-19 branch yp and the feature map X before GAP, the weight for the k-th channel of X is calculated as:

$$w_k = \frac{1}{H\,W} \sum_{i=1}^{H} \sum_{j=1}^{|W} \frac{\partial y_p}{\partial X_{i,j}^k},$$

where Xk i,j is the value at position (i, j) in the k-th channel of feature map X. Larger gradients in Eqn. (1) produce a larger
where Xk i,j is the value at position (i, j) in the k-th channel of feature map X. Larger gradients in Eqn. (1) produce a larger

$$AM_p = \sum_k ReLU(w_k X^k).$$

As shown in Fig. 9, the activation mapping accurately locates the opacification areas of COVID-19 patients, providing explainable results for the prediction of our JCS system.

ALLEVIATING DATA BIAS BY IMAGE MIXING: By utilizing our explainable classification model, our system can be trained only with patient-level annotation. However, since CT images are from multiple sources, the classifier may be trained to overfit unwanted areas (e.g., the area outside the lesion), as observed via the activation mapping. Therefore, we propose to utilize the image mixing technique [64] and help the classifier focus on the lesion areas of COVID-19 cases. The CT images from different sources and the corresponding patient-level annotations are mixed during training. Specifically, for two randomly sampled CT images xi and x j (i = j) and corresponding labels yˆi and yˆj , the newly mixed sample and the corresponding label are written as:

$$x_{ij}^m = \lambda x_i + (1 - \lambda)x_j,$$
$$\hat{y}_{ij}^m = \lambda \hat{y}_i + (1 - \lambda)\hat{y}_j,$$

where λ ∈ [0, 1] is a random number generated in Beta distribution, i.e., λ ∼ Beta(α, α). With mixed samples, our classification model is trained to focus more on the decisive lesion areas of COVID-19 cases, rather than the bias in the data source. Also, the mixing process weakens the confidence of labels, and thus alleviating our system from overfitting.

ACCURATE SEGMENTATION:

Our segmentation branch aims at discovering the exact lesion areas from the CT images of COVID-19 patients. above shows the architecture of our segmentation branch with or without the combination of the segmentation and classification models. The details of such a combination are illustrated in below figure.
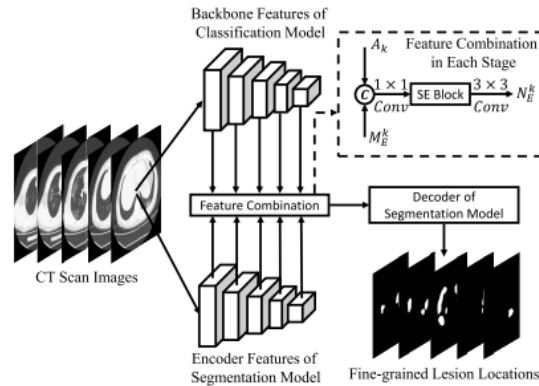

Fig 3: Combination of the segmentation and classification models.

We combine the encoder features of the segmentation model with the backbone features of the classification model.

ENCODER-DECODER ARCHITECTURE: Our segmentation model consists of an encoder and a decoder. Encoder. The encoder is based on the VGG-16 [38] backbone, without the last two fully-connected layers. It has five VGG blocks defined as {E1, E2, E3, E4, E5}, respectively. The VGG-16 backbone is first fed with the CT images and produces multi-scale feature maps from the last layers of the five VGG blocks. To downsize the input feature map by half, the front of each block (except the first one) is a max pooling function with a stride of 2. The feature map produced by the block E1 contains the finest features with the highest resolution, while the feature map by the block E5 is coarsest with the lowest resolution. To achieve better performance, we propose an Enhanced Feature Module (EFM) for our encoder to improve its representational power. The EFM module is added after the last layer conv5_3 in the block E5. It consists of two Grouped Atrous Modules (GAM) to extract stronger feature maps with larger receptive fields. The GAM module generates an extra smaller feature map, half size compared to the coarsest feature map of the VGG-16 backbone. It also enhances the representational power of the feature map produced by the block E5. Hence, our encoder produces six levels of feature maps {M1 E , M2 E , M3 E , M4 E , M5 E , M6 E }, with strides of {1, 2, 4, 8, 16, 32}, respectively. As we employ a U-shape encoder-decoder architecture [58], all these six feature maps will be used in the decoder, as will be introduced later. Decoder. Our decoder has five side-outputs with 5 different sizes. Here, we do not predict the side-output from the coarsest feature map with a stride of 32, and thus no side-output matches the size of the coarsest feature map M6 E . In our decoder, we propose an Attentive Feature Fusion (AFF) strategy to aggregate the feature maps from different stages and predict the side-output

ENHANCED FEATURE MODULE: The proposed EFM module is added after the last layer of E5 in the VGG-16 encoder. It consists of two sequential GAM modules and a max pooli ng function between them. the first layer of the GAM module is a 1×1 convolution layer to expand the channels of the feature map. Then the feature map is equally divided into 4 groups. Unlike the trivial group convolution, we deploy atrous convolution [53] with different atrous rates to the 4 groups to derive a more abundant feature map with various receptive fields. Atrous convolution can greatly enlarge the perceptive field of convolution filters and keep the same computational cost with normal convolution. In 2D cases, atrous convolution with 3×3 kernel size can be simply formulated as below:

$$q[i, j] = bias + \sum_{k=-1}^{+1} \sum_{l=-1}^{+1} (x[i + k \cdot n, j + l \cdot n] \cdot w[k + 1, l + 1]),$$

where n indicates the atrous rate, w is the convolution weight of which the size is 3×3, q and x are output and input feature map, respectively, i and j are the feature map location. Note that n = 1 is the special case for normal convolution. To fully exploit useful features, we adopt the Squeeze-Excitation (SE) block [66] in our network, that is, using the attention mechanism for re-calibrating channel-wise convolutional feature responses. More specifically, each channel of the input feature map will be multiplied by a channel factor calculated by a SE block. The SE block consists of two linear layers, followed by a sigmoid function. The input feature map after global average pooling will be fed into this block and we can derive a channel factor ranging (0, 1) for each input feature channel. We set the reduction rate in the SE block as 4, which means we set the output number of the first linear layer as the 1/4 number of the input channels. To reduce the output channels by half, we add a 1×1 convolution layer after the SE block. At last, we use a 3×3 convolution layer, in which the number of channels equals that of the input feature map, as the transition layer to the next module.

ATTENTIVE FEATURE FUSION: Traditional fusion strategy of top-down decoders [8], [6] treats the input feature maps equally. To better aggregate the feature maps, we propose an Attentive Feature Fusion (AFF) strategy. In our AFF fusion strategy, the feature map with a smaller size is more valued. As shown in Fig(b), the input feature maps M_i E and M_{i+1} D in the current stage are reduced to half size via 1×1 convolution layers. Then the reduced M_{i+1} D is up-sampled by bi-linear interpolation to output a double-sized feature map. We concatenate the two outputs and apply the SE block (also used in GAM) to produce an enhanced feature map. This feature map is then concatenated with the feature map of doubly up-sampled output in the previous stage. After the concatenation, we use another SE block to enhance the feature map again. After each SE block, we use a 3×3 convolution layer, with the same number of channels as the input, as the transition layer. A 1×1 convolution layer with a single neuron will be used to predict one feature map as the side-output of the current stage.

COMBINATION WITH THE CLASSIFICATION MODEL: As described above, we have designed two models, one for COVID-19 classification and the other one for COVID-19 opacification segmentation. However, they are separately working on the diagnosis system, and there might be a way to combine them together for better performance. Inspired by this, we leverage the features of the classification model to enhance the features of the segmentation model. As shown in Fig, we merge the feature maps of each stage from the encoder of the segmentation model and the backbone of the classification model together. The feature maps of the encoder of the segmentation model are M_1 E , M_2 E , M_3 E , M_4 E , M_5 E as defined. The Res2Net [40] backbone of the classification model has five stages and we use the last feature maps A_k of stage $k \in [1, 5]$ for the feature combination. In merging the features of stage k, we have two feature maps A_k, M_k E for the merge. We first resize the smaller one A_k, making it the same size as the larger one M_k E , and concatenate them together. Then, we apply a simple 1×1 convolution layer for the feature channel reduction, making the output feature maps the same number of channels as M_k E . Such 1×1 convolution layer is followed by a SE block with a reduction rate of 4. At last we use a 3×3 convolution layer of the same number of input and output channels as the transition layer. The output N_k E will be regarded as the enhanced encoder features and be fed into the decoder of the segmentation model.

DEEP SUPERVISION LOSS: Although the final prediction is only from the last side-output, we apply the deep supervision strategy [68] to all side-outputs with different sizes. For each side-output, we up-sample it to the size of the ground-truth map, and compute the sum of the standard binary cross-entropy loss and the Dice loss

$$L = BCE(\mathbf{P}, \mathbf{G}) + 1 - \frac{\mathbf{P} \cdot \mathbf{G}}{\|\boldsymbol{P}\|_1 + \|\boldsymbol{G}\|_1},$$

where the binary cross-entropy (BCE) loss is averaged among all $H \times W$ pixels, $p_{i,j}$ is the confidence score at pixel (i, j) calculated by a sigmoid function, and "·" means the dot product. P and G are predicted map and ground-truth map, respectively, while P_1 and G_1 denote the corresponding 1 norms.

JOINT DIAGNOSIS An explainable classifier or accurate segmentation model itself could not fully implement comprehensive functions for COVID-19 diagnosis. Comparing to the segmentation model, our classifier is trained with CT images from both COVID-19 infected and uninfected cases, benefiting from more training data with lower annotation costs. Although our classifier can provide explainable lesion location of COVID-19 through activation mapping techniques, it cannot perform accurate and complete lesion segmentation. To this end, our segmentation model further provides complementary analysis by discovering the complete lesions in the lung and estimate the severity of the COVID-19 patients. But annotating vast segmentation labels by experienced radiologists is prohibitively expensive. To integrate their advantages for better application, we develop a diagnosis system for COVID-19 via joint explainable classification and segmentation models. In practice, our classification model will first predict whether the CT images of a suspected case to be COVID-19

positive or not. If the prediction is positive, the suspected case is very likely to be infected by COVID-19. Our segmentation model will then be performed on the CT images for in-depth analysis and to discover the whole opacification areas in each CT image.

PERFORMANCE OF DETECTION VIA YOLO

Here, all images are resized to 400 X 400 from different image sizes. For correct mass detection, it is considered the masses based on extracted and ground truth of bounding region of masses. The false-positive part of images is removed for segmentation and classification models due to lack of ground truth of false masses identification. It helps to make the performance of evaluation metrics. Thus, without false detected part, segmentation and classification models are processed for evaluation. The performance of fourfold cross-validation for mass detection is mentioned in Table. Each test fold is considered for ground-truth detection. Thus YOLO detector is performed through each test fold. Initially, different origin images are collected and resize as required where the images do not lose their infected corona virus area. It also considers the infected area to be accurately detected by augmenting the image. Moreover, it also neglects the false-positive rate of ROIs before the segmentation and classification stages of the proposed model. The performance of the detection method over the test datasets is mentioned in Figures. In this figure, the infected detection results show the potential ROIs in three stages: original ROI and invert. In each test, the detected areas are correct in all tests when the infected area is identified. The detected area is also evaluated through statistical measurements such as mean and standard deviation of the infected area, as shown in Table. This table outlines reference values used to identify COVID-19 patients. This table took only three patients' statistical experimental information out of the extensive information of all patients. The false detections are also automatically identified by this detection technique. A non-infected area is identified as false detection which expresses the consistent performance of the YOLO detector. Thus the YOLO detector performed better on accuracy aspects

Fold test	Non-COVID-19		COVID-19		Total	
	True	False	True	False	True	False
1st fold	29	1	169	1	198	2
	96.66%	3.34%	99.41%	0.59%	99.00%	1.0%
2nd fold	28	2	168	2	196	4
	93.33%	6.67%	98.82%	1.18%	98.00%	2.00%
3rd fold	29	1	169	1	198	2
	96.66%	3.34%	99.41%	0.59%	99.00%	1.00%
4th fold	29	1	169	1	198	2
	96.66%	3.34%	99.41%	0.59%	99.00%	1.00%
Average (%)	95.82%	4.17%	99.26%	0.73%	98.75%	1.25%

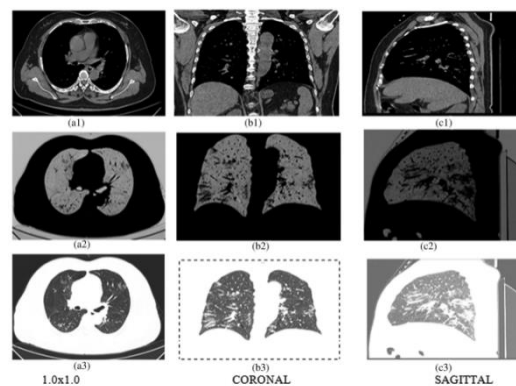TABLE 1: Mass detection over 4-fold cross-validation via YOLO

FIGURE 4: Three types of. In first row-original; second row-ROI, third row-invert of the old patient.

Segmentation performance In this part, only corrected detected masses are utilized where fourfold cross-validation is performed on all segmentation models. It also used cross-entropy as a loss function to manage several pixel numbers at the training process. The segmentation performances of the proposed FrCN are better than FCN. The quantitative evaluation is processed as per pixel of the segmented map. With the multi-scale data augmentation strategy, the boosted DSC obtains

further improvements on the Dice score, IoU. Besides, and PoolNet (Liu et al., 2019) obtained comparable results on the three metrics. U-Net performs better than DSS in terms of IoU, though they are comparable on the Dice score. One can see that the other competitors produce inaccurate or even wrong predictions of the lesion areas in the CT i.mages of mild, medium, and severe COVID-19 infections. But the proposed segmentation model correctly discovers the whole lesion areas on all levels of COVID-19 infections. In this part, the FrCN model is used to find infected pixel area segmentation during CT images. It helps to detect pixel-wise segmentation. For more stability, it performs the statistical analysis of the segmentation model on our segmentation test set. Further, it considers the correlation between the Dice score of our model and the infected areas of CT images. It also explores the relationship between the lesion count of each slice and the Dice score from different sections. The Dice score's probability distribution is little affected by the number of lesion counts in a CT image. The consistently promising performance on segmenting lesion areas and the low probability of failure confirm the stability of our segmentation model. This part uses the CNN model to get sound output by using deep hierarchical features. During CT images, it is considered up to a certain level to get the exact infected area by a virus. The classification model trained with or without image mixing is shown. The activation mapping (AM) is used for classification models trained with random horizontal flip and random crop. It not only covers the lesion areas but also presents unrelated areas. This indicates that the classification model is biased to non-lesion areas. The proposed classification model provides more precise locations of the graze areas. It considers the threshold value for the affected area of the COVID-19 patient image. When the affected area of CT images from a suspected patient is larger than a threshold, the patient is diagnosed as COVID-19 positive. Changing the threshold enables the proposed model to get a trade-off among sensitivity and specificity.
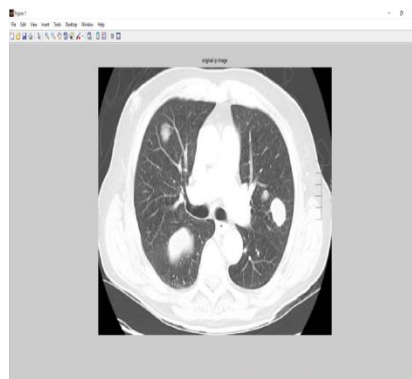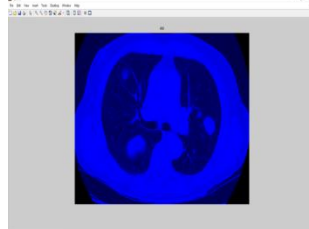
IV.RESULTS:

Fig 1: input query image

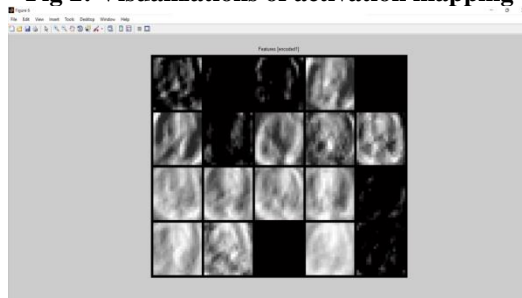**Fig 2: Visualizations of activation mapping**

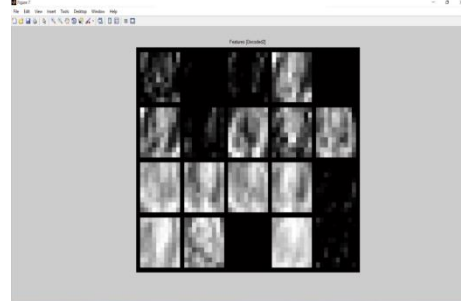**Fig 3: Features taken from query in encoded form**
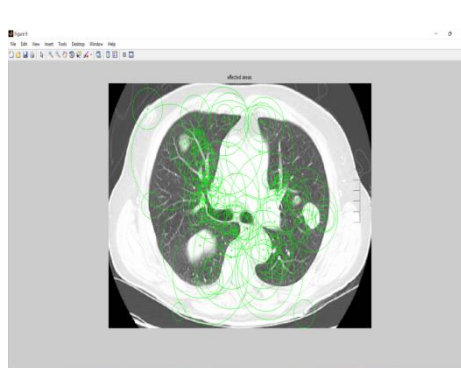
Fig 4: Features taken from query in decoded form

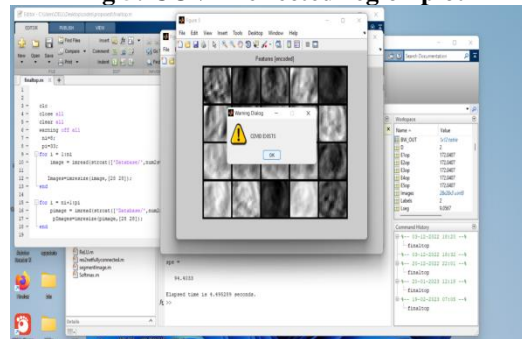**Fig 5: COVID effected region plot**

Fig 6: Final results in warning dialogue

COMPARISON TABLE:

PARAMETER	EXISTING	PROPOSED
Sensitivity	97.94%	98.94%
Specifity	89.4	94.40
Elapsed time	3.184656 seconds	1.362101 seconds

Table 2: Comparision of parameters between existing and proposed techniques.

V.CONCLUSION:

A novel method has been proposed for the efficient classification of respiratory diseases from chest CT Scan chest images. The existing technologies focus on COVID-19 diagnosis whereas this proposed method focuses on all bacterial and viral infection chest diseases. In this pandemic situation, it is necessary to differentiate COVID-19 from pneumonia. The proposed method targets preprocessing and feature descriptors to efficiently classify life-threatening chest diseases. The chest CT Scan images are preprocessed by applying various image processing algorithms. Then, the preprocessed images are subjected to transform filters with various kernels to extract predominant features of the CT Scan image. Gradient direction and magnitudes

are calculated for every pixel, and feature vectors are also extracted using histograms. YOLO-based deep learning detects several locations of the infected area. Thus, the proposed deep learning technique helps identify COVID-19 patients and provides image-based pathological area quantification.

FUTURE SCOPE:
Basic predictions of future daily incidence in Italy and Spain were estimated using the log-linear regression model for the decay phase of the outbreak. Estimates of the projected daily incidence at various time points in the future were generally found to be between two to three times larger than the true levels of daily incidence. These results highlight the fact that the estimates may only give reasonable indications in the short term, since they are based on past data which may or may not account for factors which change in the short term—e.g. new health interventions, public policy, etc.

REFERENCES
1. J. Segars, Q. Katler, D. B. McQueen et al., "Prior and novel coronaviruses, coronavirus disease 2019 (COVID-19), and human reproduction: what is known?" *Fertility and Sterility*, vol. 113, no. 6, pp. 1140–1149, 2020.View at: Publisher Site | Google Scholar
2. G. Li, R. Hu, and X. Gu, "A close-up on COVID-19 and cardiovascular diseases," *Nutrition, Metabolism and Cardiovascular Diseases*, vol. 30, no. 7, pp. 1057–1060, 2020.View at: Publisher Site | Google Scholar
3. W. Wei, D. Zheng, Y. Lei et al., "Radiotherapy workflow and protection procedures during the Coronavirus Disease 2019 (COVID-19) outbreak: Experience of the Hubei Cancer Hospital in Wuhan, China," *Radiotherapy and Oncology*, vol. 148, pp. 203–210, 2020.View at: Publisher Site | Google Scholar
4. C. Sohrabi, Z. Alsafi, N. O'Neill et al., "World Health Organization declares global emergency: a review of the 2019 novel coronavirus (COVID-19)," *International Journal of Surgery*, vol. 76, pp. 71–76, 2020.View at: Publisher Site | Google Scholar
5. R. Vaishya, M. Javaid, I. H. Khan, and A. Haleem, "Artificial intelligence (AI) applications for COVID-19 pandemic," *Diabetes & Metabolic Syndrome: Clinical Research & Reviews*, vol. 14, no. 4, pp. 337–339, 2020.View at: Publisher Site | Google Scholar
6. R. O. Panicker, K. S. Kalmady, J. Rajan, and M. K. Sabu, "Automatic detection of tuberculosis bacilli from microscopic sputum smear images using deep learning methods," *Biocybernetics and Biomedical Engineering*, vol. 38, no. 3, pp. 691–699, 2018.View at: Publisher Site | Google Scholar

7. B. Oh and J. Lee, "A case study on scene recognition using an ensemble convolution neural network," in *2018 20th International Conference on Advanced Communication Technology (ICACT)*, Chuncheon, Korea (South), 2018.View at: Google Scholar

8. C. A. Trimbak, "Analysis of image processing for digital X-ray," *International Research Journal of Engineering and Technology (IRJET)*, vol. 3, no. 5, 2016.View at: Google Scholar

9. H. Zhu, W. Sun, M. Wu, G. Guan, and Y. Guan, "Pre-processing of X-ray medical image based on improved temporal recursive self-adaptive filter," in *The 9th International Conference for Young Computer Scientists*, pp. 758–763, Hunan, China, 2008.View at: Google Scholar

10. V. Kajla, A. Gupta, and A. Khatak, "Analysis of X-Ray Images with Image Processing Techniques: A Review," in *2018 4th International Conference on Computing Communication and Automation (ICCCA)*, Greater Noida, India, 2018.View at: Publisher Site | Google Scholar

11. D. Varshni, K. Thakral, L. Agarwal, R. Nijhawan, and A. Mittal, "Pneumonia detection using CNN based feature extraction," in *IEEE International Conference on Electrical, Computer and Communication Technologies*, pp. 1–7, Coimbatore, India, 2019.View at: Google Scholar

12. K. Hammoudi, H. Benhabiles, M. Melkemi et al., "Deep learning on chest X-ray images to detect and evaluate pneumonia cases at the era of COVID-19," 2020, https://arxiv.org/abs/2004.03399.View at: Google Scholar
13. S. Rajaraman and S. Antani, "Weakly labeled data augmentation for deep learning: study on COVID-19 detection in chest X-rays," *Diagnostics*, vol. 10, no. 6, 2020.View at: Publisher Site | Google Scholar
14. V. Chouhan, S. K. Singh, A. Khamparia et al., "A novel transfer learning based approach for pneumonia detection in chest X-ray images," *Applied Sciences*, vol. 10, no. 2, 2020.View at: Publisher Site | Google Scholar

15. T. Ozturk, M. Talo, E. A. Yildirim, U. B. Baloglu, O. Yildirim, and U. Rajendra Acharya, "Automated detection of COVID-19 cases using deep neural networks with X-ray images," *Computers in Biology and Medicine*, vol. 121, article 103792, 2020.View at: Publisher Site | Google Scholar

16. G. Jain, D. Mittal, D. Thakur, and M. K. Mittal, "A deep learning approach to detect Covid-19 coronavirus with X-ray images," *Biocybernetics and Biomedical Engineering*, vol. 40, no. 4, pp. 1391–1405, 2020.View at: Publisher Site | Google Scholar

17. J. Civit-Masot, F. Luna-Perejón, M. Domínguez Morales, and A. Civit, "Deep learning system for COVID-19 diagnosis aid using X-ray pulmonary images," *Applied Sciences*, vol. 10, no. 13, 2020.View at: Publisher Site | Google Scholar

18. T. B. Chandra, K. Verma, D. K. Singh, D. Jain, and S. S. Netam, "Coronavirus disease (COVID-19) detection in chest X-ray images using majority voting based classifier ensemble," *Expert Systems with Applications*, vol. 165, article 113909, 2021.View at: Publisher Site | Google Scholar

19. J. Cohen, L. Dao, K. Roth et al., "Predicting COVID-19 Pneumonia Severity on Chest X-ray With Deep Learning," *Cureus*, vol. 12, no. 7, 2020.View at: Publisher Site | Google Scholar

20. A. Sharma, S. Rani, and D. Gupta, "Artificial intelligence-based classification of chest X-ray images into COVID-19 and other infectious diseases," *International Journal of Biomedical Imaging*, vol. 2020, Article ID 8889023, 10 pages, 2020.View at: Publisher Site | Google Scholar

21. A. S. Al-Waisy, S. Al-Fahdawi, M. A. Mohammed et al., "COVID-CheXNet: hybrid deep learning framework for identifying COVID-19 virus in chest X-rays images," *Soft Computing*, pp. 1–16, 2020.View at: Google Scholar

22. P. M. Kumar, R. Saravanakumar, A. Karthick, and V. Mohanavel, "Artificial neural network-based output power prediction of grid-connected semitransparent photovoltaic system," *Environmental Science and Pollution Research*, pp. 1–10, 2021.View at: Publisher Site | Google Scholar

23. M. A. Mohammed, K. H. Abdulkareem, A. S. al-Waisy et al., "Benchmarking methodology for selection of optimal COVID-19 diagnostic model based on entropy and TOPSIS methods," *IEEE Access*, vol. 8, pp. 99115–99131, 2020.View at: Publisher Site | Google Scholar

24. V. Chandran, M. G. Sumithra, A. Karthick et al., "Diagnosis of cervical cancer based on ensemble deep learning network using colposcopy images," *BioMed Research International*, vol. 2021, Article ID 5584004, 15 pages, 2021.View at: Publisher Site | Google Scholar

25. M. A. Mohammed, K. H. Abdulkareem, S. A. Mostafa et al., "Voice pathology detection and classification using convolutional neural network model," *Applied Sciences*, vol. 10, no. 11, 2020.View at: Publisher Site | Google Scholar

26. R. Kabilan, V. Chandran, J. Yogapriya et al., "Short-term power prediction of building integrated photovoltaic (BIPV) system based on machine learning algorithms," *International Journal of Photoenergy*, vol. 2021, Article ID 5582418, 11 pages, 2021.View at: Publisher Site | Google Scholar

27. M. K. Abd Ghani, M. K. Mohammed, M. A. Arunkumar et al., "Decision-level fusion scheme for nasopharyngeal carcinoma identification using machine learning techniques," *Neural Computing and Applications*, vol. 32, no. 3, pp. 625–638, 2020.View at: Publisher Site | Google Scholar

28. N. Y. Jayalakshmi, R. Shankar, U. Subramaniam et al., "Novel multi-time scale deep learning algorithm for solar irradiance forecasting," *Energies*, vol. 14, no. 9, p. 2404, 2021.View at: Publisher Site | Google Scholar

29. O. I. Obaid, M. A. Mohammed, M. K. A. Ghani, A. Mostafa, and F. Taha, "Evaluating the performance of machine learning techniques in the classification of Wisconsin Breast Cancer," *International Journal of Engineering & Technology*, vol. 7, pp. 160–166, 2018.View at: Google Scholar